Applied Catalysis A: General 502 (2015) 114–121

Contents lists available at ScienceDirect

Applied Catalysis A: General

journal homepage: www.elsevier.com/locate/apcata

Transition metal oxide based TiO_2 nanoparticles for visible light induced CO_2 photoreduction

Oluwafunmilola Ola*, M. Mercedes Maroto-Valer

Centre for Innovation in Carbon Capture and Storage (CICCS), School of Engineering and Physical Sciences, Heriot-Watt University, Edinburgh, EH14 4AS, United Kingdom

ARTICLE INFO

Article history:
Received 6 March 2015
Received in revised form 8 June 2015
Accepted 9 June 2015
Available online 16 June 2015

Keywords:
Visible light
Photocatalysis
Titanium dioxide
CO_2 reduction
Transitional metals

ABSTRACT

The development of nanostructured visible light photocatalytic systems capable of harnessing the energy from the sun is imperative for producing carbon based fuels and chemicals. V-, Cr- and Co-TiO_2 photocatalysts immobilized onto quartz plates were successfully prepared by sol–gel method, investigated as a function of metal concentration and tested for visible light induced CO_2 reduction for the first time. Results established that introduction of these metal ions into the host framework not only modified the crystallinity of TiO_2, but influenced its light absorption properties as well. Enhanced bathochromic shift from the UV region to longer wavelengths in the visible light region was observed with increasing metal concentrations for all samples especially Cr. The photoconversion rates were remarkably enhanced by the metal doped TiO_2 supports when compared to pure TiO_2, with the Co-TiO_2 samples having the highest photoconversion rates.

1. Introduction

Alternative fuels and chemicals produced from the photocatalytic conversion of CO_2 using H_2O is a means of addressing global energy demands without contributing to existing net CO_2 emissions. However, since CO_2 is a chemically stable compound, its conversion to carbon based fuels requires substantial input of energy. Renewable carbon free sources like solar energy can provide readily available and intermittent light irradiation required for driving this conversion process. The enormous challenge here is improving conversion efficiency to make the process economically viable and this has led to extensive research on the development of highly efficient photocatalysts and scalable reactor designs capable of effective photon utilization for catalyst activation. Photocatalytic reduction of CO_2 requires catalysts that are active under a wide light spectrum to ensure effective harnessing of light energy. However, the utilization of widely available catalysts i.e. TiO_2 (cut-off band width of anatase corresponds to 387.5 nm) for visible light applications can only be achieved by modifying its electronic properties with metal or metal oxide amongst other techniques. Apart from these metals possessing their own catalytic activity and reducing the band width, they also serve as a source of charge-carrier traps which can increase the life span of separated electron hole pairs, and thus enhance the efficiency and product selectivity for CO_2 photoreduction [1,2]. At high concentrations, these metal dopants might act as recombination centres and so decrease activity due to photon absorption of TiO_2 being blocked by metal dopants [1]. The amount and type of metal or its oxide incorporated into TiO_2 structure as well as the method of synthesis are key factors in determining photocatalytic activity and the extent of red shift that can be achieved in the visible light region. Commercialization of CO_2 photocatalytic reduction requires not only scientific insight into photocatalyst morphology and configuration but also a deep understanding of engineering aspects of these processes, upon which reliable photoreactor designs can be developed. The configuration of catalyst particles in a photoreactor system for CO_2 reduction where reaction products generated from the contact between photocatalysts, reactants and photons is also another important factor that can influence the overall photocatalytic efficiency [3,4]. An ideal photoreactor utilised in CO_2 photoreduction reactions must have uniform light distribution throughout the entire system in order to achieve optimum results. Currently, fixed bed photoreactors that employ various structured supports are found to be attractive for CO_2 reduction instead of fluidized photoreactors, where separation of catalyst particles from the reaction mixture is a major drawback [5–8]. Product selectivity and rate from CO_2 photocatalytic reduction with H_2O has been reported to be improved when catalysts were immobilized onto fixed substrates such as optical fibres, monoliths and beads amongst others [9,10]. The size of the catalyst crystals or aggregates (0.05 μm to a few μm) determines the nature of separation process required which could be expensive and time consuming [6,11]. Furthermore, the

* Corresponding author.
E-mail address: O.O.Ola@hw.ac.uk (O. Ola).

http://dx.doi.org/10.1016/j.apcata.2015.06.007

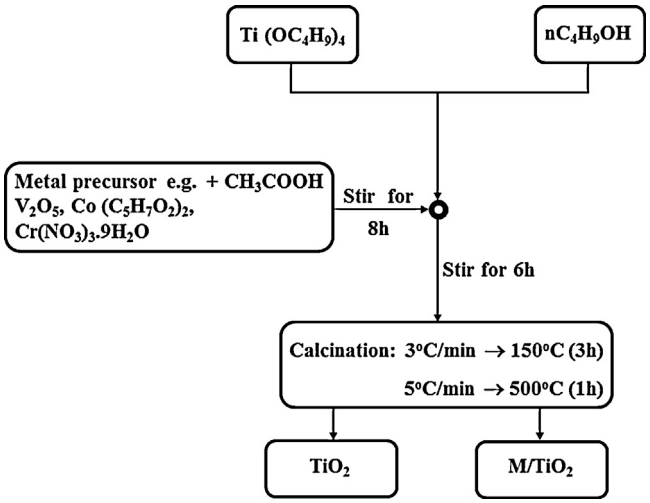

Fig. 1. Schematic of sol–gel procedure.

penetration depth of UV light into the reaction medium can also be limited by the strong light absorption of organic species and catalyst particles [4,12]. The performance comparison between Pd/Rh loaded TiO_2 suspended in H_2O or immobilized onto ceramic honeycomb monoliths (supports) was demonstrated by Ola et al. [7] for CO_2 photoreduction. The quantum efficiency of the fixed bed reactor was an order of magnitude higher than the fluidized photoreactor. Recently, CO_2 photoreduction was performed in a fixed bed reactor containing nickel based photocatalysts deposited on a quartz plate or monolith with a network of optical fibres as light guides [13]. The effect of catalyst carriers in facilitating improved light distribution was clearly established since higher product rates were observed over the quartz plate compared to the coated monoliths. The use of transparent materials like glass meets the aforementioned challenges with the material having dual functions of supporting the catalyst and promoting light delivery. Therefore, in this work quartz will be used as the light propagating material for the glass plate due to its excellent light transmission properties and stability. Composites of V-, Cr- and Co doped TiO_2 have not only shown 'red shift' in the absorption spectra in the visible light region, but also enhanced degradation of organic compounds [14–16] and photocatalytic water splitting [17,18]. However, V- and Co doped TiO_2 has not been studied for the photocatalytic reduction of CO_2 using H_2O as a reductant. Accordingly, in this work we describe the effect and synthesis of V-, Cr and Co–TiO_2 photocatalysts immobilized onto quartz plates for visible light induced CO_2 photoreduction with H_2O. The photocatalytic activity of the sol–gel derived samples were investigated as a function of metal concentration and compared to pure TiO_2.

2. Experimental

2.1. Sol–gel synthesis of metal oxide based TiO_2 nanoparticles

As shown in Fig. 1, different metal oxide based TiO_2 (M–TiO_2) nanoparticles were synthesized by the sol–gel method using vanadium (V) oxide (V_2O_5, Fisher Scientific), cobalt (II) acetylacetonate ($Co(C_5H_7O_2)_2$, Acros Organics) and chromium (III) nitrate nonahydrate ($Cr(NO_3)_3.9H_2O$, Acros Organics) as metal precursors. Pure TiO_2 sol was prepared without the addition of the metal precursors. Titanium (IV) butoxide and n-butanol in a volume ratio of 1:4 was stirred at 100 rpm for 16 h. Subsequently, metal precursors dissolved in acetic acid (to provide 0.1–2.0 wt% M–TiO_2) were added to the solution containing both titanium (IV) butoxide and n-butanol drop wise. The resulting solutions were magnetically stirred at 60 rpm for 6 h in order to allow esterification reactions take place. After 6 h, the homogeneous sol was then placed in a clean crucible and dried in a furnace (Carbolite, CWF 1100) under airflow at the rate of 3 K/min to 423 K for 3 h. The samples were further calcined to burn off organic compounds and complete crystallization at a heating rate of 5 K/min to 773 K for 1 h. The resulting samples were crushed into powder using a mortar and pestle to obtain metal oxide based TiO_2 nanoparticles of varying loading ratios.

2.2. Characterization of nanoparticles

Powder X-ray diffraction was performed on the Hiltonbrooks X-ray powder diffractometer with a Philips PW 1050 goniometer and proportional detector. Phase identification was carried out using the MDI Jade 5.0 traces v.3 processing software while the crystallite size was computed using the Scherrer's equation ($d = k\lambda/\beta \cos\theta$) where d is the crystallite size, k is a constant, β is the full width at half maximum (FWHM) intensity of the (1 0 1) peak in radians, and θ is Bragg's diffraction angle. The strain/disorder contributions to reflection widths and anisotropic effects on coherent diffraction domain size were not considered during calculation of the crystallite size. Surface morphology and elemental composition of the catalysts were examined by using scanning electron microscopy and energy dispersive spectroscopy (SEM-EDS, Quanta 600 model) for measuring the emitted X-rays after scanning a section of the compacted pellets by an electron beam (15 eV). The high vacuum mode and voltage of 30 kV was used during SEM while the low vacuum mode and voltage of 25 kV was used for the SEM–EDS. The morphology and particle size distribution of the samples were studied by TEM. TEM analysis was conducted using a JEOL 2100F instrument at an acceleration voltage at 200 kV. Absorption spectra of powder samples recorded in the form of wavelength plotted against absorbance (intensity of the light) was measured by using a spectrometer (Varian Cary 300). The threshold wavelength was determined by the extrapolation of the absorption edge (i.e. the region where the absorbance has a maximum increase with respect to the wavelength) and the baseline (i.e. the region where little or no change in absorbance is observed with respect to increasing wavelength). Diffuse reflectance was recorded using a Perkin Elmer Lambda 950 UV/Vis/NIR spectrometer with a diffuse reflectance accessory. Diffuse reflectance UV-vis spectra were obtained using Kubelka-Munk function of $F(R) = (1\text{-}R)^2/2R$, where R is reflectance (%). Tauc plot was then obtained from the equation of $(F(R)\,hv)^{1/n} = A(hv\text{-}Eg)$, where hv, A and n represents photon energy, band gap and electron transition during absorption process. Bandgap was estimated from the point where the linear portion of the plot intersected the y axis. Due to the spectra overlapping, spectra were shifted on the y-axis for clarity and comparison purposes. The specific surface area was determined by the adsorption of an inert gas (nitrogen, N_2) using a ChemBET TPR/TPD analyser connected to a linear mass flow controller/gas blender. X-ray photoelectron spectroscopy (XPS) was performed by using a Kratos AXIS ULTRA with a mono-chromated Al kα X-ray source (1486.6 eV) typically operated at 25 mA emission current and 12 kV anode potential. The high resolution scans were charge corrected to the main C 1s peak = 285 eV and subsequently quantified to determine the amounts of each element present based on the peak areas, using CASAXPS software with Kratos sensitivity factors.

2.3. Photocatalytic CO_2 reduction

Photocatalytic reaction of CO_2 with H_2O in the gaseous phase was conducted in a cylindrical Pyrex glass reactor with dimensions of 5.5 cm × 11 cm (diameter and height). The humidifier was connected before the gas inlet, while the temperature and pressure were monitored via a type T thermocouple and pressure gauge,

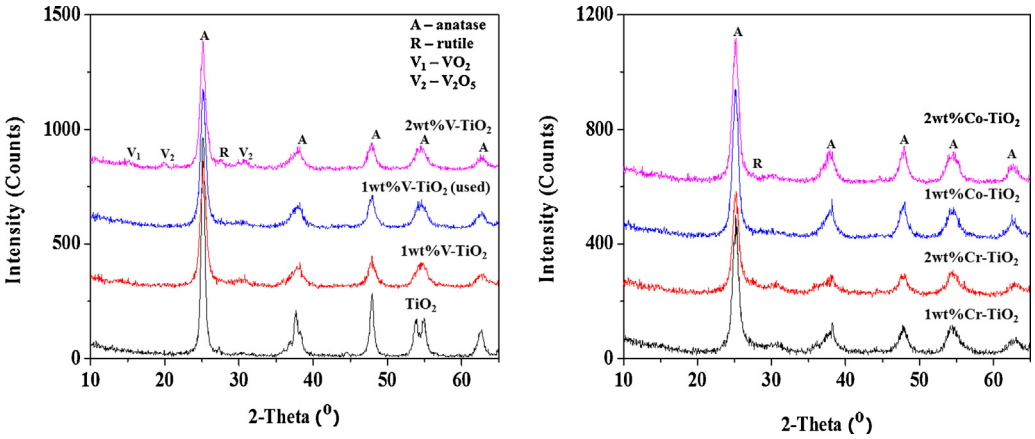

Fig. 2. XRD diffraction patterns of pure TiO_2, 1 wt%V–TiO_2 (fresh and used), 2 wt%V–TiO_2, 1 wt%Cr–TiO_2, 2 wt%Cr–TiO_2, 1 wt%Co–TiO_2 and 2 wt%Co–TiO_2.

respectively, connected by 1/8" fittings after the product outlet. Approximately 0.2 g of catalyst was evenly dispersed on the quartz plate with dimensions of 4.5 cm × 10.5 cm which was inclined at an angle of 15° facing the light rays emitted through the quartz window (Fig. S1). The surface of the quartz plate was roughened by sandblasting to provide strong adherence between the catalyst and the support. The assembled photoreactor was placed in a gloved box to avoid external light interference. Leakage was tested by observing changes in the pressure gauge when purging with helium (He) gas. If leak-proof, the reactor was then purged with He for 1 h to eliminate residual air, then switched to CO_2 (Air Products, 99.9995%) gas saturated with water vapour for 1 h at flow rate of 4 ml/min. The pressure was maintained at 1 bar to increase the solubility of the CO_2 in the system. After 1 h, the light source was turned on to activate the catalysts and readings were taken after 4 h. Halogen lamp (500 W) with wavelength distribution within the range of 380–1100 nm irradiated the catalyst through the quartz window. The light intensity was measured by a radiometer (R2000, Omnicure) at 6 different positions. The average light intensity was 68.35 mW/cm^2. Light irradiation was transmitted into the photoreactor via the quartz window present in front of the photoreactor. Circulating cooling water was applied to control the rise in temperature of the lamp during use. The reaction was performed in batch mode. Gas stream were analysed using a mass spectrometer (MS, Hiden Analytical) equipped with capillary, quadrupole mass analyser (HAL 201-RC) and Faraday/Secondary electron multiplier (SEM) detectors. Each gas compound was determined by using a unique mass and ionization profile assigned after the spectral overlaps were resolved by the software. Individual gas compounds were identified using specifically assigned mass distribution keys where the green-coloured boxes represent the peaks suitable for analysis after the spectral overlap was resolved by the software, while the grey-coloured boxes represent the peaks where the spectral overlap could not be resolved (Table S1). The green-coloured boxes were therefore chosen for identifying individual gas compounds, and the respective masses under which they were present were the specific masses chosen for compound identification. The software automatically calculated and subtracted the spectral overlap before providing quantitative analysis. The resulting data from calibration were used by MASsoft Professional for subsequent experimental runs. The results were displayed as they were acquired in tabular format as ppm. An average of 3 readings was used from 3 experimental runs. Although CO production has been reported in the literature, CO could not be detected with our standard HPR-20 system, because CO_2 is the bulk gas [9]. This results in a large CO^+ (m/z\28) background signal arising from CO_2 fragmentation. Control experiments were performed with and without the light source in the presence and absence of the catalyst to confirm that reactions were due to CO_2 photoreduction. The CO_2 reduction experiments were repeated thrice, with the production rates averaged and the error bars reported. Series of background test were conducted to prove that carbon based compounds originated from CO_2 photoreduction. First series of tests were performed in the absence or presence of several parameters such as light source; H_2O, catalyst and CO_2. Further tests were also conducted using pure helium or argon as a substitute for CO_2. The presence of hydrocarbons was not identified in the aforementioned conditions, which demonstrates that CO_2 photoreduction cannot proceed without the presence of H_2O, CO_2, catalyst and light.

3. Results and discussion

3.1. Textural properties of M–TiO_2 photocatalysts

Fig. 2 presents the X-ray diffraction patterns of pure TiO_2 and V-, Cr-, and Co-based TiO_2 nanoparticles after calcination at 773 K. The

Table 1
Physicochemical properties of sol–gel derived M-TiO_2 nanoparticles.

M-TiO_2 samples	Crystallite size (nm)/phase content (%)		S_{BET} (m^2/g)[a]	XPS (at%)[b]	Band gap (eV)
	Anatase	Rutile			
TiO_2	13.8	–	40.7	–	3.0
1.0 wt% V–TiO_2	12.2	–	100.2	1.9	1.9
2.0 wt% V–TiO_2	11.3 (88.2)	25.1 (11.8)	106.4	4.9	1.7
1.0 wt% Cr–TiO_2	11.8	–	120.2	0.1	2.8
2.0 wt% Cr–TiO_2	10.4 (90.3)	8.6 (9.7)	62.2	0.4	2.1
1.0 wt% Co–TiO_2	11.2	–	99.1	2.1	2.7
2.0 wt% Co–TiO_2	10.1	–	106.4	5.8	2.4

[a] BET specific surface area.
[b] Atomic percentages of metals estimated from peak areas in XPS spectra.

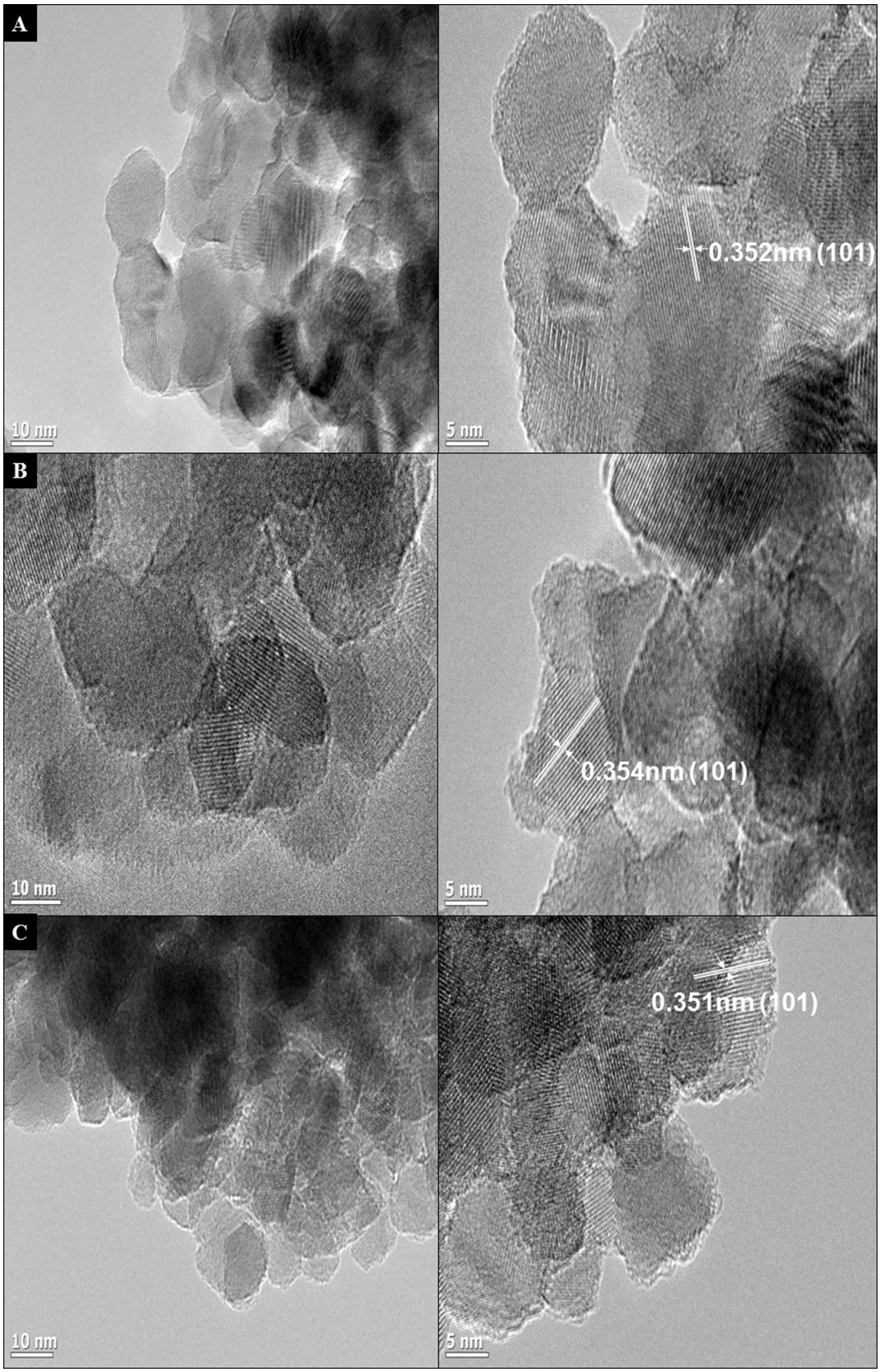

Fig. 3. TEM micrographs of 1 wt%V–TiO_2 (A), 1 wt%Cr–TiO_2 (B) and 1 wt%Co–TiO_2 (C).

loading ratios were set at 1 wt% and 2 wt% for each element. The crystalline phase of all samples was primarily anatase. Rutile peaks at ca. 27.4° and 36.1° (JCPDS Card File No.65-0191) were further observed in the diffraction pattern of 2 wt%V- and 2 wt%Cr–TiO_2 samples only. Chromium and cobalt peaks in its metal or oxide phase were not observed even at the highest loading ratio of 2 wt% within the XRD detection limits. Additional peaks belonging to vanadium in its metal or oxide phase were also not observed in samples with loading ratios within 0.1–1.5 wt%. As shown in Fig. 1, the phase structures of V elements on the surface of 2 wt%V–TiO_2 photocatalyst were observed by the characteristic diffraction peaks of vanadium (IV) oxide (VO_2) at ca. 14.9° and 29.9° (JCPDS Card File No.42-0876) and vanadium (V) oxide (V_2O_5) at ca. 20.3° and 31.0° (JCPDS Card File No.42-0876). A similar trend was observed by Li et al. [19] and Zhao et al. [20] for their $Ti_{1-x}V_xO_2$ films. The peaks of rutile and V_2O_5 were observed when $x = 2$ and $x = 0.25$ for the sol gel derived films calcined at 773 K and 973 K, respectively [19,20]. The crystallite grain size for anatase calculated from the Scherrer equation for the metal based samples were within 10.1–13.8 nm (Table 1). The crystallize size of anatase for the metal based TiO_2 samples slightly decreased with increasing metal concentration compared to crystallite size of pure TiO_2 (Table 1). No other crystalline phase was detected from the XRD pattern of 1 wt%V–TiO_2 before and after photocatalytic reaction (Figure 2). An increase in specific surface area of TiO_2 occurs with an increase in V concentration and surface area values were within the range of 100.2 106.4 m^2/g. The BET specific surface area of the Cr–TiO_2 based photocatalysts were within the range of 62.2–120.2 m^2/g while specific surface area of the Co–TiO_2 based photocatalysts were within the range of 99.1–106.4 m^2/g. Fig. S2 show the surface morphology of TiO_2 nanoparticles. Aggregates of spherical shaped particles of varying sizes were observed from the SEM micrographs of pure TiO_2 nanoparticles using the magnification of 140,000 ×. After calcination at 773 K for 1 h, nearly spherical nanoparticles of varying diameters from 6–31 nm were observed from the transmission electron microscopy (TEM) micrographs (Fig. 3a–c). The high resolution (HR) TEM images of the samples indicate that the samples were crystalline in nature. The interplanar crystal spacing of 0.351–0.354 nm for the M–TiO_2 nanoparticles corresponds to the 1 0 1 plane of anatase TiO_2.

3.2. XPS analysis

The near surface elemental composition of the M-TiO_2 samples measured by XPS are listed in Table 1 while high resolution XPS spectra of V 2p and Co 2p of 2 wt%M-TiO_2 nanoparticles calcined at 773 K are presented in Fig. 4. In Fig. 4a, the binding energies at 517.4 eV and 524.4 eV are characteristic of vanadium (IV) oxide while the binding energies at 516.3 eV and 525.1 eV are characteristic of vanadium (V) oxide, respectively [21]. This indicates that V species exist in the TiO_2 matrix in the form of V^{4+} and V^{5+}. These values are consistent with the binding energies of V $2p_{3/2}$ measured for V doped TiO_2 [14]. The presence of V^{4+} species in the sol gel derived vanadium doped TiO_2 samples were probably due to the reduction of V^{5+} by the decomposition of organics from starting materials [22,23]. The V 2p peaks of the fresh and used catalysts occur at the same binding energies before and after the photocatalytic reaction (Fig. 4a). In Figure S3, the binding energies of the Cr $2p_{3/2}$ and Cr $2p_{1/2}$ core levels at 576.5 eV and 586.3 eV are characteristic of chromium (III) oxide, respectively [24]. This indicates that Cr species exist predominantly in the TiO_2 lattice sites in the form of Cr^{3+}. These values are consistent with the binding energies of Cr $2p_{3/2}$ measured for Cr doped TiO_2 [16,25,26]. As shown in Fig. 4b, the binding energy of the Co $2p^{1/2}$ core level at 796.4 eV and Co $2p_{3/2}$ core level at 780.4 eV are characteristic of cobalt (II)

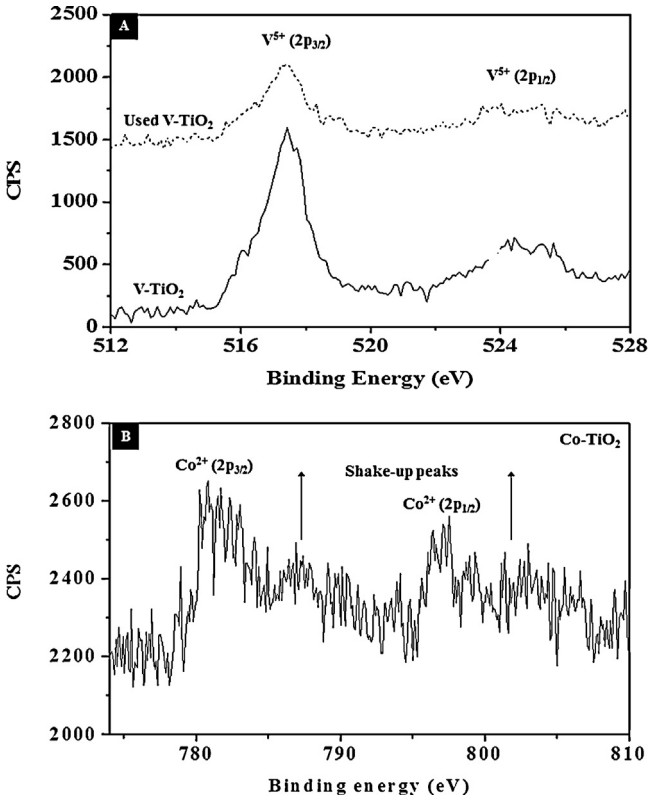

Fig. 4. XPS spectra of V 2p (A) and Co 2p (B) of M–TiO_2 samples.

oxide, respectively [24]. The shake-up satellite peaks of Co $2p_{3/2}$ and Co $2p_{1/2}$ which are characteristic of the high spin Co^{2+} are also present at binding energies of 786.1 eV and 802.5 eV, respectively. This indicates that Co species exist in the TiO_2 lattice sites in the form of Co^{2+}. These values are consistent with the binding energies of Co $2p_{3/2}$ and Co $2p_{1/2}$ measured for Co doped TiO_2 [27,28]. The peaks of Ti $2p_{3/2}$ and Ti $2p_{1/2}$ for all M–TiO_2 samples are located at 458.8 eV and 464.7 eV respectively, which agree well with the values reported in the literature for anatase TiO_2 [24].

3.3. Light absorption properties of M-TiO_2 photocatalysts

The absorption spectra for the M–TiO_2 samples synthesized by the sol–gel method at various loading ratios are presented in Fig. 5. Addition of V, Cr and Co ions results in a red shift of the absorption edges and decrease in band gap energies of these M–TiO_2 based samples when compared with the spectrum of pure TiO_2 (3.1 eV). Absorption spectra of the resulting M–TiO_2 photocatalysts showed increased shift in the visible light with increased metal concentration. The largest shift of the absorption edge was observed by the 2 wt% of all samples within the series tested; with Cr-TiO_2 samples having the lowest band gap energies followed by the V- and Co–TiO_2 samples (Fig. 5). The increased absorbance shown by all the samples may arise from the charge transfer transition from the 3d orbitals of the metal ions to the TiO_2 conduction band [29]. The optical properties of TiO_2 were tuned towards the visible light by the substitution of Ti^{4+} by V^{4+} or V^{5+} ions. Several researchers have reported that the absorption band of V^{4+} is centred at 770 nm, while the absorption band of V^{5+} is lower than 570 nm [23,29]. Based on the spectra of the V-based photocatalysts in this study, it can be inferred that both V^{4+} and V^{5+} ions coexist in the samples, which is consistent with XRD and XPS results. The tailings observed in the absorption band of M–TiO_2 samples have been reported to be assigned to the charge transfer transition from the 3d orbitals of

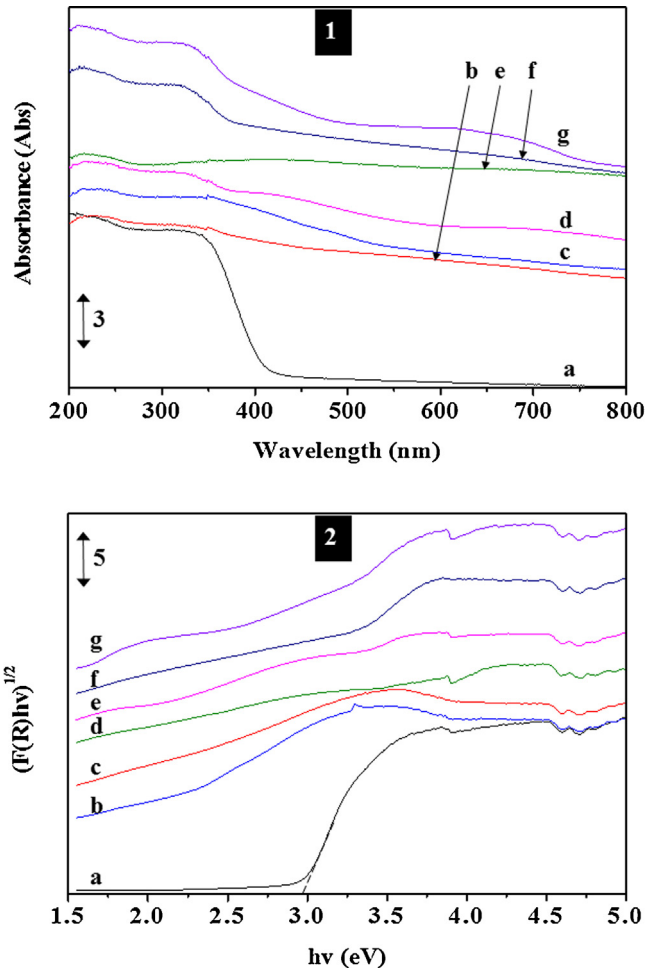

Fig. 5. (1) UV–vis absorption spectra and (2) corresponding plot of Kubelka-Munk function versus photon energy of (a) TiO_2, (b) 1 wt%V–TiO_2, (c) 2 wt%V–TiO_2, (d) 1 wt%Cr–TiO_2, (e) 2 wt%Cr–TiO_2, (f) 1 wt% Co–TiO_2 and (g) 2 wt% Co–TiO_2.

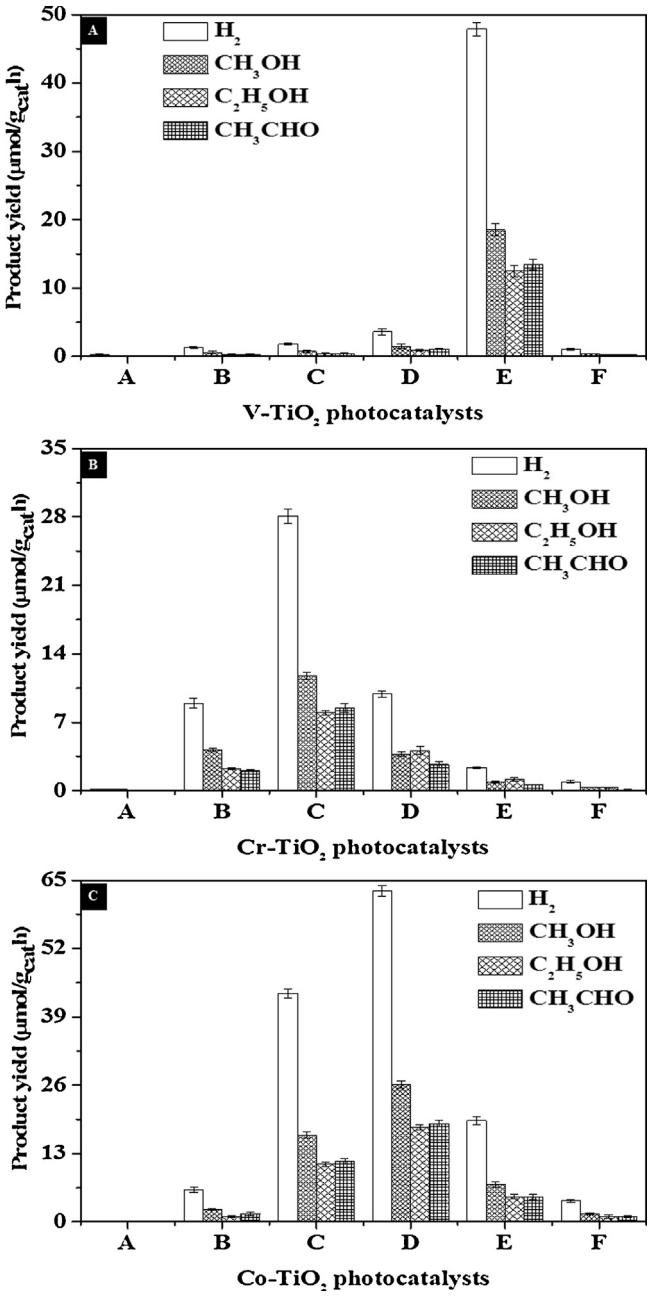

Fig. 6. Effect of metal concentration on product rate using quartz plate as a catalyst carrier under visible light irradiation (A-pure TiO_2, B-0.1 wt%, C-0.5 wt%, D-1 wt%, E-1.5 wt% and F-2 wt%).

metal species to the TiO_2 conduction band [21,29,30]. For Cr-TiO_2, the band gap energies of the Cr-based catalysts were within the range of 2.12–2.94 eV, while the band gap energies were within the range of 2.51–3.04 eV for Co–TiO_2 samples. These results are consistent with the previous findings where the addition of Cr and Co species results in a red shift of the absorption edges and decrease in band gap energies of the TiO_2 based samples when compared to pure TiO_2 [15,28,31].

3.4. Photocatalytic reduction of CO_2

The effect of various M–TiO_2 based photocatalysts dispersed on the quartz plates for photocatalytic CO_2 reduction using visible light irradiation for 4 h is illustrated in Fig. 6. In this study, hydrogen, methanol, acetaldehyde and ethanol were identified as the main products during photoreaction. Although CO production has been reported in the literature, CO could not be detected in our experiments with our standard HPR-20 system. As shown in Fig. 6a, the product rates steadily increases until it reached the maximum for vanadium loading of 1.5 wt% and decreases for the subsequent higher loading ratio under visible light. Maximum product rates of 47.89 $\mu mol/g_{cat}h$ and 18.49 $\mu mol/g_{cat}h$, were obtained for hydrogen and methanol evolution over the V–TiO_2 catalysts dispersed on the quartz plates. Cr–TiO_2 samples showed optimum photocatalytic activity at loading ratio of 0.5 wt% within the series tested. The maximum product rate of 28.08 $\mu mol/g_{cat}h$ and 11.74 $\mu mol/g_{cat}h$ for hydrogen and methanol production decreased for subsequent higher loading ratios after 4 h of visible light irradiation (Fig. 6b). The photocatalytic activity was increased up to a maximum product rate of 62.91 $\mu mol/g_{cat}h$ and 26.12 $\mu mol/g_{cat}h$ for hydrogen and methanol, respectively for the 1 wt%Co–TiO_2 sample (Fig. 6c). All M–TiO_2 based samples show a much higher level of photoactivity than pure TiO_2. Hydrogen and methanol were favourably produced in the gas phase for all M–TiO_2 based samples because two and six photoelectrons were required for their formation, respectively. Overall, maximum hydrogen and methanol production was observed over TiO_2 doped with Co^{2+} ions in comparison with other M-TiO_2 photocatalysts within the series tested. Fig. 7 shows the effect of irradiation time on the product rate using the optimal catalyst, 1 wt%Co–TiO_2 catalyst dispersed on the quartz plate under visible light irradiation. Production rate steadily increases till the

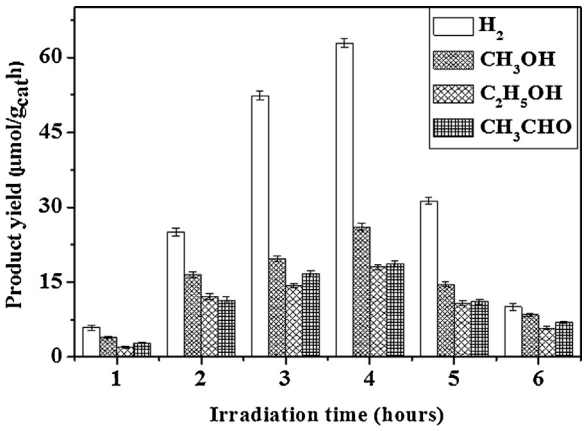

Fig. 7. Irradiation time profile of 1 wt%Co–TiO_2.

4th hour, after which decline in product formation was observed for the subsequent hours.

Several researchers have used different glass substrates for CO_2 reduction under UV light [32,33]. Highly dispersed titanium oxide anchored onto Vycor glass was prepared by Anpo et al. [34] for the photocatalytic reduction of CO_2 with H_2O. The supports were prepared through facile reaction between surface OH groups of a transparent porous Vycor glass and $TiCl_4$. UV irradiation of the support led to the formation of C1 compounds such as CH_4, CH_3OH and CO as major products and trace amounts of C_2 compounds (C_2H4 and C_2H_6) at 323 K. Cu nanoparticles were deposited on fluorinated tin oxide (FTO) glass substrates for CO_2 reduction to CH_4 under UV irradiation [35]. Cu–TiO_2 films (~0.18 μmol/g h) were reported to exhibit higher rates compared to pure TiO_2 (~0.07 μmol/g h) and TiO_2 P25 (~0.01 μmol/g h). Enhanced light absorption and increased diffusion length of photoinduced electrons were amongst some of the reasons for enhanced CO_2 photoconversion rates. Platinum (Pt)-TiO_2 nanostructured thin films with different deposition times were immobilized onto indium tin oxide (ITO)-coated aluminumosilicate glass using RF magnetron sputtering and gas-phase deposition method [36]. The films which had a one-dimensional (1D) structure of TiO_2 single crystals with ultrafine Pt nanoparticles (NPs, 0.5–2 nm) produced CO (179 μmol/g_{cat}h) and CH_4 (1361 μmol/g_{cat}h) under UV light irradiation. The fast electron-transfer rate in TiO_2 single crystals and the efficient electron–hole separation by the Pt NPs were the main reasons reported to be attributable for this enhancement. The results of this study can only be indirectly compared to the research by Nishimura et al. [37,38] where series of sol–gel derived Cr–TiO_2 coated quartz discs were tested for CO_2 photoreduction under visible light. Under their experimental conditions, the Cr-doped TiO_2 samples showed improved photoresponse in the visible light in their study compared to the pure TiO_2 film. Optimum product yield of 1.89 mmol/gcat (CO) was obtained using 70 wt%Cr–TiO_2 immobilized on top of the quartz disc after 96 h of visible light irradiation. A comparison between their results and this present study established the contributing effect of Cr in enhancing CO_2 reduction performance of TiO_2 in the visible light region. Product formation rate cannot be directly compared due to the absence of CO detection capability in this present study.

The increased visible light absorption and specific surface area upon addition of V, Cr and Co were key factors that influenced the photocatalytic activity of these photocatalysts in the visible light region compared to pure TiO_2. The reduction in crystallite size and higher surface areas when compared to pure TiO_2 also facilitated improved photocatalytic efficiency due to their large surface to volume ratios which reduces the probability of electron–hole recombination [12]. Several researchers have reported that V^{4+} species were the active sites on V based TiO_2 catalysts for the photodegradation of ethene [21], toluene [39] and methylene blue [40]. Furthermore, it is generally accepted that V^{4+} can act as both an electron and hole trap and thus charge separation can be favoured by the charge transfer transition from V^{4+} to the conduction band of Ti^{4+} level, while V^{5+} can serve as an electron acceptor only [39,41]. The substitution of Ti^{4+} with increasing Cr atoms in the crystal lattice causes lattice deformation owing to the rearrangement of the neighbouring atoms compensating for charge deficiency. This charge compensation effect results in the generation of oxygen vacancies during calcination [31]. Conduction-band edge of VO_2, V_2O_5 and CoO nanocrystals have been reported to be above the hydrogen evolution potential of −0.41 V, while the valence band edge lies below the oxygen-evolution potential [42,43]. Photogenerated electrons and holes react with H^+ and OH^- ion dissociated from surface adsorbed H_2O molecules to form adsorbed hydrogen and OH radical [9]. Further reaction of holes with $^{\bullet}CO_2^-$ radicals and H led to the formation of hydrocarbons as the final product. The influence of these substitutional ions is further confirmed by the change in light absorption properties of the Cr- and Co based TiO_2 samples observed in the UV–vis spectra when compared to pure TiO_2. The incorporation of these metal ions in TiO_2 matrix can increase the optical absorption towards the visible light region which subsequently facilitates the photocatalytic activity of TiO_2 in the visible light. The light absorption properties of the photocatalysts were extended towards the visible light region upon the addition of V, Cr and Co, which implies that the formation of photogenerated charge carriers will be enhanced. The increased red shift and optical absorption observed in the visible light region was due to defect centres created by the substitution of Ti^{4+} with increasing metal ions in the crystal lattice of TiO_2. Therefore, the band gap energy required for the migration of valence band electrons to the conduction band is reduced, leading to the availability of more photogenerated charge carriers to participate in the reduction of CO_2. Based on the CO_2 photoreduction results presented above, it is therefore evident that photoreduction is strongly dependent on the metal concentration rather than the band width of the metal based TiO_2 photocatalysts. These photogenerated electrons and holes then undergo redox reactions with the electron donors and acceptors adsorbed on the surface of TiO_2 to derive fuels as demonstrated in this study. However, increased recombination rate of the photogenerated charge carriers may increase with high metal concentration due to metal ion species acting as both electron and hole traps and thus creating multiple trap sites.

Similar trend of reduced photoactivity after exceeding the optimum metal concentration has been reported in the literature and our previous studies [44,45]. Probable causes are attributed to the coverage of the surface of TiO_2 with increased metal ions which can inhibit interfacial charge transfer due to insufficient amount of light energy available for activation of all the catalyst particles. The increased concentration of V ions can also act as recombination centres of holes and electrons. Bhattacharyya et al. [21] observed maximum conversion rates using 5 mol%V doped TiO_2 sample, after which drastic reduction was observed for the 10 mol% sample. The decline in activity was ascribed to presence of excess V ions facilitating the increased electron generation and the narrowed band width probably contributing to reverse electron transfer and hole quenching. When the metal content of Cr exceeded 0.2 wt%, Zhu et al. [26] recorded a decrease in photocatalytic dye degradation due to electron hole recombination. Hamadanian et al. [15] observed maximum degradation rates using 0.5 wt%Co doped TiO_2 sample, after which the degradation rates of methyl orange decreased for the other samples. The decrease in photocatalytic activity was ascribed to Co particles

acting as recombination centres for photogenerated electrons and holes.

4. Conclusions

M–TiO_2 photocatalysts immobilized onto quartz plates were successfully prepared by sol–gel process and tested for the photocatalytic reduction of CO_2 under visible light irradiation for the first time. The addition of varying concentrations of V, Cr and Co in TiO_2 sol resulted in a decrease in crystallite size of anatase and enhancement of the optical absorption to longer wavelengths in the visible light region. Results showed that the photoconversion rates were remarkably enhanced for the M-doped TiO_2 supports when compared to pure TiO_2 at optimal metal concentrations, with the Co–TiO_2 samples having the highest photoconversion rates. Conversely, high metal concentration was detrimental to visible light photocatalytic activity, likely due to the metal ion species acting as multiple trap sites and thus facilitating electron–hole recombination. Experimental results obtained from the sol–gel derived M–TiO_2 based supports can be further optimized to improve CO_2 reduction efficiency for future applications.

Acknowledgements

The authors thank the financial support provided by the School of Engineering and Physical Sciences and the Centre for Innovation in Carbon Capture and Storage (EPSRC grant number EP/K021796/1) at Heriot-Watt University.

Appendix A. Supplementary data

Supplementary data associated with this article can be found, in the online version, at http://dx.doi.org/10.1016/j.apcata.2015.06.007

References

[1] A.L. Linsebigler, G. Lu, J.T. Yates Jr., Chem. Rev. 95 (1995) 735–758.
[2] D. Liu, Y. Fernández, O. Ola, S. Mackintosh, M. Maroto-Valer, C.M.A. Parlett, A.F. Lee, J.C.S. Wu, Catal. Commun. 25 (2012) 78–82.
[3] M. Bideau, B. Claudel, C. Dubien, L. Faure, H. Kazouan, J. Photochem. Photobiol. A 91 (1995) 137–144.
[4] A.K. Ray, A.A. Beenackers, Catal. Today 40 (1998) 73–83.
[5] A.E. László Guczi, Catalysis for Alternative Energy Generation, Springer, New York, 2012.
[6] M. Bouchy, O. Zahraa, Int. J. Photoenergy 5 (2003) 191–197.
[7] O. Ola, M. Maroto-Valer, D. Liu, S. Mackintosh, C.-W. Lee, J.C. Wu, Appl. Catal. B Environ. 126 (2012) 172–179.
[8] O. Ola, M.M. Maroto-Valer, Catal. Sci. Tech. 4 (2014) 1631–1637.
[9] M. Tahir, N.S. Amin, Appl. Catal. A Gen. 467 (2013) 483–496.
[10] T.V. Nguyen, J.C.S. Wu, Sol Energy Mater. Sol. Cells 92 (2008) 864–872.
[11] M. Schiavello, Heterogeneous Photocatalysis, Wiley, Chichester, 1997.
[12] T.V. Nguyen, J.C.S. Wu, Appl. Catal. A Gen. 335 (2008) 112–120.
[13] O. Ola, M. Mercedes Maroto-Valer, J. Catal. 309 (2014) 300–308.
[14] J.C.-S. Wu, C.-H. Chen, J. Photochem. Photobiol. A 163 (2004) 509–515.
[15] M. Hamadanian, A. Reisi-Vanani, A. Majedi, J. Iran. Chem. Soc. 7 (2010) S52–S58.
[16] S. Zhang, Y. Chen, Y. Yu, H. Wu, S. Wang, B. Zhu, W. Huang, S. Wu, J. Nanopart. Res. 10 (2008) 871–875.
[17] C.-C. Pan, J.C. Wu, Mater. Chem. Phys. 100 (2006) 102–107.
[18] D. Wu, H. Tong, Q. Chen, C. Xia, Integr. Ferroelectr. 127 (2011) 55–62.
[19] H. Li, G. Zhao, G. Han, B. Song, Surf. Coat. Technol. 201 (2007) 7615–7618.
[20] G. Zhao, H. Kozuka, H. Lin, T. Yoko, Thin Solid Films 339 (1999) 123–128.
[21] K. Bhattacharyya, S. Varma, A. Tripathi, S. Bharadwaj, A. Tyagi, J. Phys. Chem. C 112 (2008) 19102–19112.
[22] S. Liu, T. Xie, Z. Chen, J. Wu, Appl. Surf. Sci. 255 (2009) 8587–8592.
[23] X. Yang, C. Cao, K. Hohn, L. Erickson, R. Maghirang, D. Hamal, K. Klabunde, J. Catal. 252 (2007) 296–302.
[24] A.V.N. C. D. Wagner, A. Kraut-Vass, J. W. Allison,C. J. Powell and J. R. Rumble, NIST X-ray Photoelectron Spectroscopy Database 20 Version 4.1., 2012.
[25] Y.-H. Peng, G.-F. Huang, W.-Q. Huang, Adv. Powder Technol. 23 (2012) 8–12.
[26] J. Zhu, F. Chen, J. Zhang, H. Chen, M. Anpo, J. Photochem. Photobiol. A 180 (2006) 196–204.
[27] C. Huang, X. Liu, Y. Liu, Y. Wang, Chem. Phys. Lett. 432 (2006) 468–472.
[28] C. Shifu, L. Wei, Z. Sujuan, C. Yinghao, J. Sol–Gel Sci. Technol. 54 (2010) 258–267.
[29] X. Yang, F. Ma, K. Li, Y. Guo, J. Hu, W. Li, M. Huo, Y. Guo, J. Hazard. Mater. 175 (2010) 429–438.
[30] B. Tian, C. Li, F. Gu, H. Jiang, Y. Hu, J. Zhang, Chem. Eng. J. 151 (2009) 220–227.
[31] B. Tian, C. Li, J. Zhang, Chem. Eng. J. 191 (2012) 402–409.
[32] O. Ozcan, F. Yukruk, E.U. Akkaya, D. Uner, Appl. Catal. B Environ. 71 (2007) 291–297.
[33] E.G. Look, H.D. Gafney, J. Phys. Chem. A 117 (2013) 12268–12279.
[34] M. Anpo, H. Yamashita, Y. Ichihashi, S. Ehara, J. Electroanal. Chem. 396 (1995) 21–26.
[35] J.Z. Tan, Y. Fernández, D. Liu, M. Maroto-Valer, J. Bian, X. Zhang, Chem. Phys. Lett. 531 (2012) 149–154.
[36] W.-N. Wang, W.-J. An, B. Ramalingam, S. Mukherjee, D.M. Niedzwiedzki, S. Gangopadhyay, P. Biswas, J. Am. Chem. Soc. 134 (2012) 11276–11281.
[37] A. Nishimura, N. Komatsu, G. Mitsui, M. Hirota, E. Hu, Catal. Today 148 (2009) 341–349.
[38] A. Nishimura, G. Mitsui, K. Nakamura, M. Hirota, E. Hu, Int. J. Photoenergy 2012 (2011).
[39] A. Kubacka, A. Fuerte, A. Martinez-Arias, M. Fernandez-Garcia, Appl. Catal. B Environ. 74 (2007) 26–33.
[40] D.-E. Gu, B.-C. Yang, Y.-D. Hu, Catal. Lett. 118 (2007) 254–259.
[41] K.L. Schulte, P.A. DeSario, K.A. Gray, Appl. Catal. B Environ. 97 (2010) 354–360.
[42] V.P. Indrakanti, J.D. Kubicki, H.H. Schobert, Energ. Environ. Sci. 2 (2009) 745–758.
[43] T.F.-R. Shen, M.-H. Lai, T.C.-K. Yang, I.-P. Fu, N.-Y. Liang, W.-T. Chen, J. Taiwan Inst. Chem. E 43 (2012) 95–101.
[44] R. Dholam, N. Patel, A. Miotello, Int. J. Hydrogen Energy 36 (2011) 6519–6528.
[45] N. Serpone, D. Lawless, J. Disdier, J.-M. Herrmann, Langmuir 10 (1994) 643–652.